Astronomy & Astrophysics manuscript no. GJ536_AA_vArxiv
November 8, 2016

A super-Earth orbiting the nearby M-dwarf GJ 536

A. Suárez Mascareño[1, 2], J. I. González Hernández[1, 2], R. Rebolo[1, 2, 3], N. Astudillo-Defru[4], X. Bonfils[5, 6], F. Bouchy[4], X.Delfosse[5, 6], T. Forveille[5, 6], C. Lovis[4], M. Mayor[4], F. Murgas[5, 6], F. Pepe[4], N. C. Santos[7, 8], S. Udry[4], A. Wünsche[7, 8], and S. Velasco[1, 2]

[1] Instituto de Astrofísica de Canarias, E-38205 La Laguna, Tenerife, Spain
e-mail: `asm@iac.es`
[2] Universidad de La Laguna, Dpto. Astrofísica, E-38206 La Laguna, Tenerife, Spain
[3] Consejo Superior de Investigaciones Científicas, Spain
[4] Observatoire Astronomique de l'Université de Genève, Versoix, Switzerland
[5] Univ. Grenoble Alpes, IPAG, Grenoble, France
[6] CNRS, IPAG, Grenoble, France
[7] Instituto de Astrofísica e Ciências do Espaço, Universidade do Porto,CAUP, Rua das Estrelas, 4150-762 Porto, Portugal
[8] Departamento de Física e Astronomia, Faculdade de Ciências,Universidade do Porto,Rua Campo Alegre, 4169-007 Porto, Portugal

Written July-2016

ABSTRACT

We report the discovery of a super-Earth orbiting the star GJ 536 based on the analysis of the radial-velocity time series from the HARPS and HARPS-N spectrographs. GJ 536 b is a planet with a minimum mass M sin *i* of 5.36 ± 0.69 $M_\oplus$ with an orbital period of 8.7076 ± 0.0025 days at a distance of 0.066610(13) AU, and an orbit that is consistent with circular. The host star is the moderately quiet M1 V star GJ 536, located at 10 pc from the Sun. We find the presence of a second signal at 43 days that we relate to stellar rotation after analysing the time series of Ca II H&K and H_α spectroscopic indicators and photometric data from the ASAS archive. We find no evidence linking the short period signal to any activity proxy. We also tentatively derived a stellar magnetic cycle of less than 3 years.

Key words. Planetary Systems — Techniques: radial velocity — Stars: activity — Stars: chromospheres — Stars: rotation — Stars: magnetic cycle — starspots — Stars: individual (GJ 536)

1. Introduction

Several surveys have attempted to take advantage of the low masses of M-dwarfs – and therefore of the stronger radial-velocity signals induced for the same planetary mass – and closer habitable zones to detect rocky habitable planets (Bonfils et al. 2013; Howard et al. 2014; Irwin et al. 2015; Berta-Thompson et al. 2015a). While surveying M-dwarfs has advantages, it also has its own drawbacks. Stellar activity has been one of the main difficulties when trying to detect planets trough Doppler spectroscopy. Not only it introduces noise, but also coherent signals that can mimic those of planetary origin (Queloz et al. 2001; Bonfils et al. 2007; Robertson et al. 2014). M-dwarfs tend to induce signals with amplitudes comparable to those of rocky planets (Howard et al. 2014; Robertson et al. 2014). While these kinds of stars allow for the detection of smaller planets, they also demand a more detailed analysis of the radial-velocity signals induced by activity. In addition this low mass stars offer valuable complementary information on the formation mechanisms of planetary systems. For instance giants planets are known to be rare around M dwarfs, while on the other hand super-Earths appear to be more frequent (Bonfils et al. 2013; Dressing & Charbonneau 2013; Dressing et al. 2015).

In spite of the numerous exoplanets detected by *Kepler* (Howard et al. 2012) and by radial-velocity surveys (Howard et al. 2009; Mayor et al. 2011) the number of known small rocky planets is still comparably low. There are around 1500 confirmed exoplanets and more than 3000 Kepler candidates, but only about a hundred of the confirmed planets have been reported on M-dwarfs and only a fraction of them are rocky planets. The first discovery of a planet around an M-dwarf dates back to 1998 (Delfosse et al. 1998; Marcy et al. 1998). Since then several planetary systems have been reported containing Neptune mass planets and super-Earths (Udry et al. 2007; Delfosse et al. 2013; Howard et al. 2014; Astudillo-Defru et al. 2015) even some Earth-mass planets (Mayor et al. 2009; Berta-Thompson et al. 2015b; Wright et al. 2016; Affer et al. 2016). However the frequency of very low-mass planets around M-dwarfs is not well established yet. In particular, as noted by Bonfils et al. (2013), the frequency of rocky planets at periods shorter than 10 days is $0.36^{+0.24}_{-0.10}$, being $0.41^{+0.54}_{-0.13}$ for the habitable zone of the stars. On the other hand Gaidos (2013) estimated that the frequency of habitable rocky planets is $0.46^{+0.20}_{-0.15}$ on a wider spectral sample of Kepler dwarfs and Kopparapu (2013) gave a frequency of $0.48^{+0.12}_{-0.24}$ for habitable planets around M-dwarfs. The three measurements are compatible, but uncertainties are still big making it important to continue the search for planets around this type of stars in order to refine the statistics.

We present the discovery of a super-Earth orbiting the nearby star GJ 536, which is a high proper motion early M-dwarf at a distance of 10 pc from the Sun (van Leeuwen 2007; Maldonado et al. 2015). Because of its high proper motion and its closeness this star shows a secular acceleration of 0.24 m s^{-1} yr^{-1} (Montet

Table 1: Stellar parameters of GJ 536

Parameter	GJ 536	Ref.
RA (J2000)	14:01:03.19	1
DEC (J2000)	-02:39:17.52	1
δ RA(mas yr^{-1})	-823.47	1
δ DEC (mas yr^{-1})	598.19	1
Distance [pc]	10.03	1
m_B	11.177	2
m_V	9.707	2
m_V ASAS	9.708	0
Spectral Type	M1	3
T$_{\rm eff}$ [K]	3685 ± 68	3
$[Fe/H]$	-0.08 ± 0.09	3
$M_\star$ [$M_\odot$]	0.52 ± 0.05	3
$R_\star$ [$R_\odot$]	0.50 ± 0.05	3
log g (cgs)	4.75 ± 0.04	3
$\log(L_\star/L_\odot)$	-1.377	3
$\log_{10}(R'_{\rm HK})$	-5.12 ± 0.05	0
$P_{\rm rot}$	45.39 ± 1.33	0
$v \sin i$ (km s^{-1})	$< 1.2^*$	0
Secular acc. (m s^{-1} yr^{-1})	0.24	4

References: 0 - This work, 1 - van Leeuwen (2007), 2 - Koen et al. (2010), 3 -Maldonado et al. (2015), 4 - Calculated following Montet et al. (2014).

* Estimated using the Radius estimated by Maldonado et al. (2015) and our period determination.

et al. 2014). Table 1 shows the stellar parameters. Its moderately low activity combined with its long rotation period, of more than 40 days (Suárez Mascareño et al. 2015), makes it a very interesting candidate to search for rocky planets.

1.1. Spectroscopy

The star GJ 536 is part of the Bonfils et al. (2013) sample and has been extensively monitored since mid-2004. We have used 146 HARPS spectra taken over 11.7 yr along with 12 HARPS-N spectra taken during April and May 2016. HARPS (Mayor et al. 2003) and HARPS-N (Cosentino et al. 2012) are two fibre-fed high resolution echelle spectrographs installed at the 3.6 m ESO telescope in La Silla Observatory (Chile) and at the Telescopio Nazionale Galileo in the Roque de los Muchachos Observatory (Spain), respectively. Both instruments have a resolving power greater than $R \sim 115\,000$ over a spectral range from ~380 to ~690 nm and have been designed to attain very high long-term radial-velocity accuracy. Both are contained in vacuum vessels to avoid spectral drifts due to temperature and air pressure variations, thus ensuring their stability. HARPS and HARPS-N are equipped with their own pipeline providing extracted and wavelength-calibrated spectra, as well as RV measurements and other data products such as cross-correlation functions and their bisector profiles.

Most of the observations were carried out using the Fabry Perot (FP) as simultaneous calibration. The FP offers the possibility of monitoring the instrumental drift with a precision of 10 cms^{-1} without the risk of contamination of the stellar spectra by the ThAr saturated lines (Wildi et al. 2010). While this is not usually a problem in G and K stars, the small amount of light collected in the blue part of the spectra of M-dwarfs might compromise the quality of the measurement of the Ca II H&K flux. The FP allows a precision of $\sim$ 1 ms^{-1} in the determination of the radial velocities of the spectra with highest signal to noise while assuring the quality of the spectroscopic indicators even in those spectra with low signal to noise. Measurements taken before the availability of the FP where taken without simultaneous reference.

1.2. Photometry

We also use the photometric data on GJ 536 provided by the All Sky Automated Survey (ASAS) public database. ASAS (Pojmanski 1997) is an all sky survey in the V and I bands running since 1998 at Las Campanas Observatory, Chile. Best photometric results are achieved for stars with V ~8-14, but this range can be extended implementing some quality control on the data. ASAS has produced light-curves for around 10^7 stars at $\delta < 28°$. The ASAS catalogue supplies ready-to-use light-curves with flags indicating the quality of the data. For this analysis we relied only on good quality data (grade "A" and "B" in the internal flags). Even after this quality control, there are still some high dispersion measurements which cannot be explained by a regular stellar behaviour. We reject those measurements by de-trending the series and eliminating points deviating more than three times the standard deviation from the median seasonal value. We are left with 359 photometric observations taken over 8.6 yr with a typical uncertainty of 9.6 mmag per exposure.

2. Determination of Stellar Activity Indicators and Radial Velocities

2.1. Activity Indicators

For the activity analysis we use the extracted order-by-order wavelength-calibrated spectra produced by the HARPS and HARPS-N pipelines. For a given star, the change in atmospheric transparency from day to day causes variations in the flux distribution of the recorded spectra that are particularly relevant in the blue where we intend to measure Ca II lines. In order to minimize the effects related to these atmospheric changes we create a spectral template for each star by de-blazing and co-adding every available spectrum and use the co-added spectrum to correct the order-by-order fluxes of the individual ones. We also correct each spectrum for the Earth's barycentric radial velocity and the radial velocity of the star using the measurements given by the standard pipeline and re-binned the spectra into a wavelength-constant step. Using this HARPS dataset, we expect to have high quality spectroscopic indicators to monitor tiny stellar activity variations with high accuracy.

S_{MW} Index

We calculate the Mount Wilson S index and the $\log_{10}(R'_{HK})$ by using the original Noyes et al. (1984) procedure, following Lovis et al. (2011) and Suárez Mascareño et al. (2015). We define two triangular-shaped passbands with full width half maximum (FWHM) of 1.09 Å centred at 3968.470 Å and 3933.664 Å for the Ca II H&K line cores, and for the continuum we use two 20 Å wide bands centred at 3901.070 Å (V) and 4001.070 Å(R), as shown in figure 1.

Then the S-index is defined as

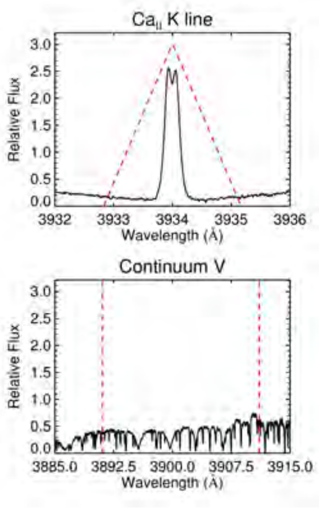

Fig. 1: Ca II H&K filter of the spectrum of the star GJ536 with the same shape as the Mount Wilson Ca II H&K passband.

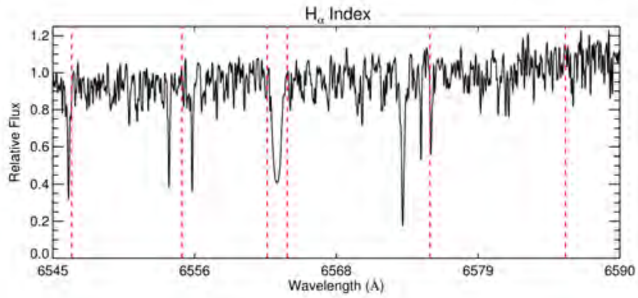

Fig. 2: Spectrum of the M-type star GJ536 showing the Hα filter passband and continuum bands.

$$S = \alpha \frac{\tilde{N}_H + \tilde{N}_K}{\tilde{N}_R + \tilde{N}_V} + \beta, \qquad (1)$$

where $\tilde{N}_H, \tilde{N}_K, \tilde{N}_R$ and $\tilde{N}_V$ are the mean fluxes in each passband, while α and β are calibration constants fixed as $\alpha = 1.111$ and $\beta = 0.0153$. The S index serves as a measurement of the Ca II H&K core flux normalized to the neighbour continuum. As a normalized index to compare it to other stars we compute the $\log_{10}(R'_{\rm HK})$ following Suárez Mascareño et al. (2015).

H_α Index

We also use the Hα index, with a simpler passband following Gomes da Silva et al. (2011). It consists of a rectangular bandpass with a width of 1.6 Å and centred at 6562.808 Å (core), and two continuum bands of 10.75 Å and a 8.75 Å wide centred at 6550.87 Å (L) and 6580.31 Å (R), respectively, as seen in Figure 2.

Thus, the Hα index is defined as

$$H\alpha_{\rm Index} = \frac{H\alpha_{\rm core}}{H\alpha_L + H\alpha_R}. \qquad (2)$$

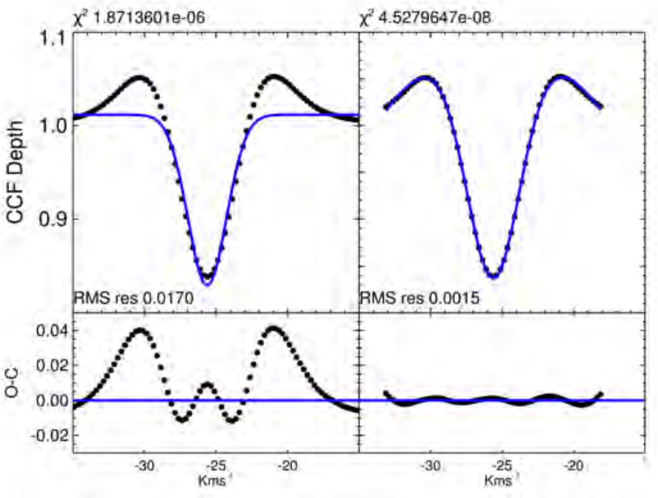

Fig. 3: Cross correlation function for GJ 536. Upper panels show the CCF with the Gaussian fit (left) and our Gaussian plus polynomial fit (right). Lower panels show the residuals after the fit for the Gaussian fit (left) and for our fit. Blue lines show the fit (upper panels) and the zero line (lower panels).

2.2. Radial velocities

The radial-velocity measurements in the HARPS standard pipeline is determined by a Gaussian fit of the cross correlation function (CCF) of the spectrum with a binary stellar template (Baranne et al. 1996; Pepe et al. 2000). In the case of M-dwarfs, due to the huge number of line blends, the cross correlation function is not Gaussian resulting in a less precise gaussian fit which might cause distortions in the radial-velocity measurements and FWHM To deal with this issue we tried two different approaches.

The first one consisted in using a slightly more complex model for the CCF fitting, a Gaussian function plus a second order polynomial (Fig. 3) using only the central region of the CCF function. We use a 15 Km s^{-1} window centred at the minimum of the CCF. This configuration provides the best stability of the measurements. Along with the measurements of the radial velocity we obtain the FWHM of the cross correlation function which we also use to track variations in the activity level of the star. A second approach to the problem was to recompute the radial velocities using a template matching algorithm with a high signal to noise stellar spectral template (Astudillo-Defru et al. 2015). Every spectrum is corrected from both barycentric and stellar radial velocity to align it to the frame of the solar system barycenter. The radial velocities are computed by minimizing the χ^2 of the residuals between the observed spectra and shifted versions of the stellar template, with all the elements contaminated by telluric lines masked. All radial-velocity measurements are corrected from the secular acceleration of the star.

For the bisector span measurement we rely on the pipeline results, as it does not depend on the fit but on the CCF itself. The bisector has been since more than 10 years ago a standard activity diagnostic tool for solar type stars. Unfortunately its behaviour in slow rotating stars is not as informative as it is for fast rotators (Saar & Donahue 1997; Bonfils et al. 2007). We report the measurements of the bisector span (BIS) for each radial-velocity measurement, but we do not find any meaningful information in its analysis.

2.3. Quality Control of the Data

As the sampling rate of our data is not well suited for modelling fast events, such as flares, and their effect in the radial velocity is not well understood, we identify and reject points likely affected by flares by searching for an abnormal behaviour of the activity indicators (Reiners 2009). The process rejected 6 spectra that correspond to flare events of the star with obvious activity enhancement and line distortion. That leaves us with 140 HARPS spectroscopic observations taken over 10.7 years, with most of the measurements taking place after 2013, with a typical exposure of 900 s and an average signal to noise ratio of 56 at 5500 Å. We do not apply the quality control procedure to the HARPS-N data as the number of spectra is not big enough.

3. Stellar Activity Analysis

In order to properly understand the behaviour of the star, our first step is to analyse the different modulations present in the photometric and spectroscopic time-series.

We search for periodic variability compatible with both stellar rotation and long-term magnetic cycles. We compute the power spectrum using a Generalised Lomb Scargle Periodogram (Zechmeister & Kürster 2009) and if there is any significant periodicity we fit the detected period using sinusoidal model, or a double harmonic sinusoidal model to account for the asymmetry of some signals (Berdyugina & Järvinen 2005), with the MPFIT routine (Markwardt 2009).

The significance of the periodogram peak is evaluated using both the Cumming (2004) modification of the Horne & Baliunas (1986) formula to obtain the spectral density thresholds for a desired false alarm probability (FAP) levels and bootstrap randomization (Endl et al. 2001) of the data.

Figure 4 shows the time series for the photometry (top panel) and the three activity proxies (bottom panels) used for this analysis. The periodograms of both the photometric and FWHM time series show significant signals at ~40 days, compatible with the typical rotation periods of low activity M1 stars (Suárez Mascareño et al. 2016; Newton et al. 2016). On the other hand the periodograms of the S_{MW} and H_α indexes show long term and short term significant signals. The short period signal is again at ~40 days while the long term signal is close to ~1000 days.

3.1. Long Term Magnetic Cycle

Analysing the S_{MW} and H_α indexes time series we find the presence of a long term magnetic cycle of ~3 years. Figure 5 shows the periodograms of the time series of both indexes. We see a well defined peak in the S_{MW} index periodogram at ~806 d and several peaks going from ~600 d to 1100 d in the H_α index periodogram implying the shape of the cycle is still not well defined within our observations. Table 2 shows the periods of the best fits for both time series using least squares minimization with the period corresponding to the highest peak of the periodogram as initial guess. Figure 6 shows the phase folded curves using these periods. The two estimates differ significantly. This might be because of a sub-optimal sampling to detect signals of long periods. The detected periodicities might not be the true periodicities, but apparent periodicities close to the real one, caused by the sampling. This also makes us think that the uncertainties in the cycle length are underestimated. The length of the signal is shorter than the typical magnetic cycles measured in solar type stars, but is within the range of known magnetic cycles in M-type stars (Suárez Mascareño et al. 2016). Both in the S_{MW} and H_α indexes it seems that the cycle shape shows a quick rise followed by a slow decline, as it is the case in the Sun and many other main sequence stars (Waldmeier 1961; Baliunas et al. 1995). Unfortunately this cycle is not well covered in phase yet, making it difficult to properly characterise it. More observations are needed in order to better constrain its period.

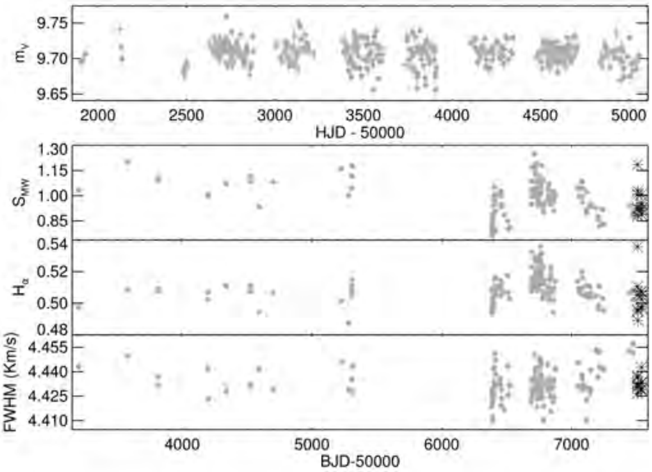

Fig. 4: Time series of the m_V (upper panel) , S_{MW} index (upper-mid panel), H_α index (lower-mid panel) and FWHM (lower panel) time series. Grey dots show HARPS-S data, black asterisks show HARPS-N data.

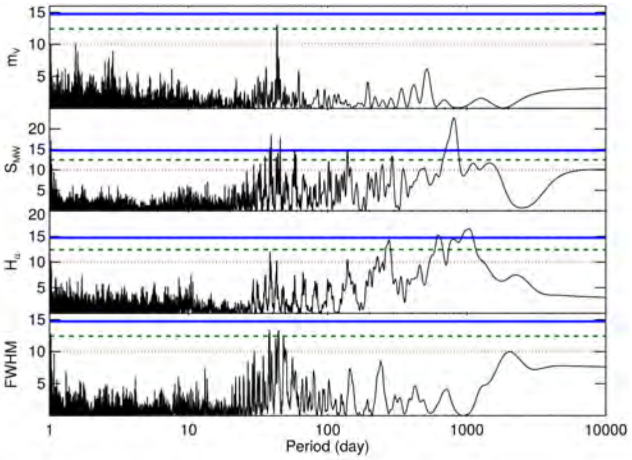

Fig. 5: Periodograms of the m_V (upper panel) , S_{MW} index (upper-mid panel), H_α index (lower-mid panel) and FWHM (lower panel) time series. Horizontal lines show the different levels of false alarm probability. Red dotted line for the 10% of false alarm probability, greed dashed line for the 1% and blue thick line for the 0.1%. Several peaks arise with significances better than the 0.1%.

3.2. Rotation

The other activity signal expected in our data is the rotational modulation of the star.It shows up at ~43 d with a false alarm probability smaller or close to the 1% in the four time series (Fig. 5) that grow in significance after removing the long term effects.

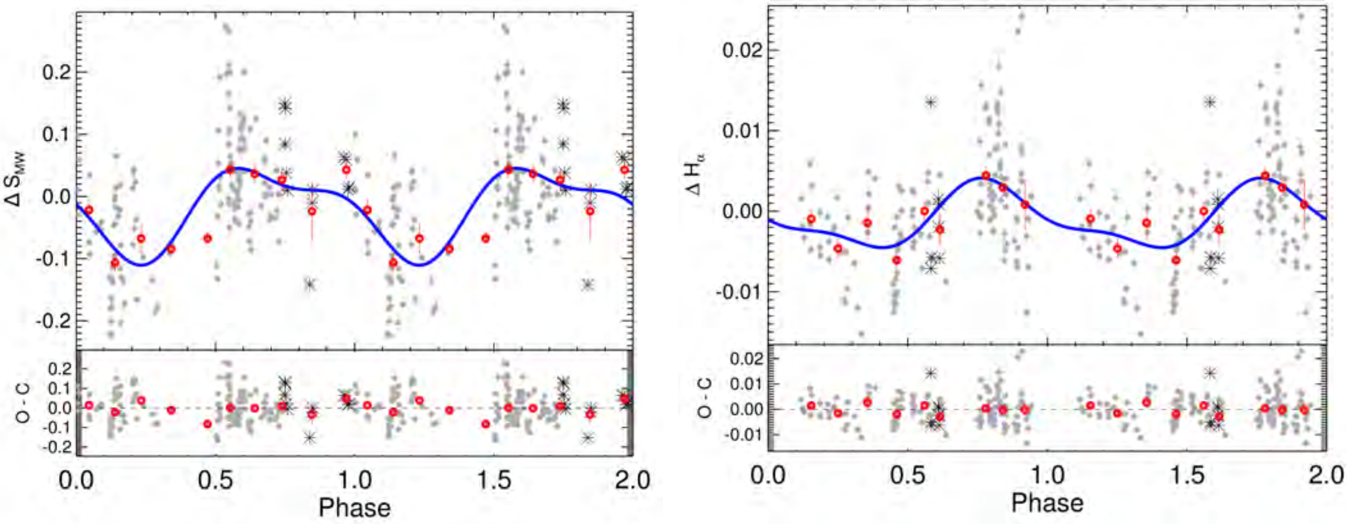

Fig. 6: Phase folded fit for the isolated long period activity signal using double-harmonic sine curves. Left panel shows the S$_{MW}$ index data using the 824 d signal while right panel shows the H$_\alpha$ signal using the 1075 d signal. Grey dots are the raw measurements after subtracting the mean value. Red dots are the same points binned in phase with a bin size of 0.1.

In the photometric lightcurve we measure a modulation of 43.33 ± 0.06 d with an amplitude of 5.21 ± 0.68 mmag. For the S$_{MW}$ index we find a signal 43.84 ± 0.01 d with an amplitude of 0.0628 ± 0.0010 when doing a simultaneous fit with the ~824 days signal from Table 6. In the case of the H$_\alpha$ index we find a signal 42.58 ± 0.08 d with an amplitude of 0.0042 ± 0.0010, also when doing a simultaneous fit with the ~1075 days signal. The time series of the FWHM show a linear increase with time of ~ 2 ms^{-1}yr^{-1}, which might be related to a slow focus drift of HARPS. After subtracting the linear trend we find again a periodicity of 44.47 ± 0.03 d period with an amplitude of 4.56 ± 0.31 ms^{-1}. Figure 7 shows the phase folded fits of all the signals. The S$_{MW}$ index and FWHM signals seem to be in phase, while the photometric signal is shifted a quarter of phase. The uncertainty in the H$_\alpha$ long term fit makes it difficult to give it a unique phase to the rotation signal. Table 2 shows the parameters for the four signals.

Our measurement of 45.39 d strengthens the previous estimation of Suárez Mascareño et al. (2015). Having such a clear detection of the rotational modulation in that many indicators over so many years supports the idea that activity regions in at least some M-type stars are stable over long time spans (Robertson et al. 2015).

4. Radial-velocity Analysis

Our 152 radial-velocity measurements have a median error of 1.33 ms^{-1} which includes both photon noise, calibration and telescope related errors. We measure a total systematic radial velocity of -25.622 Kms^{-1} with a dispersion of 3.28 ms^{-1}. Figure 8 shows the measured radial velocities. An F-test (Zechmeister et al. 2009) returns a negligible probability that the internal errors explain the measured dispersion, smaller than the 0.1%.

To search for periodic radial-velocity signals in our time-series we follow a similar procedure as the one explained in section 3.1. We search for periodic signals using a Generalised Lomb Scargle Periodogram and if there is any significant periodicity we fit the detected signal using the RVLIN package (Wright & Howard 2012). We sequentially find the dominant component

Table 2: Magnetic cycle and rotation periodicities

Series	Period (d)	Amplitude	FAP (%)
S$_{MW\ \mathrm{Cyc}}$	824.9 ± 1.7	0.0684 ± 0.0011	< 0.1
H$_{\alpha\ \mathrm{Cyc}}$	1075.8 ± 36.1	0.0046 ± 0.0011	< 0.1
m$_{V\ \mathrm{Rot}}$	43.33 ± 0.06	5.21 ± 0.68 mmag	< 1
S$_{MW\ \mathrm{Rot}}$	43.84 ± 0.01	0.0628 ± 0.0010	< 0.1
H$_{\alpha\ \mathrm{Rot}}$	42.58 ± 0.08	0.0042 ± 0.0010	< 0.1
FWHM$_{\mathrm{Rot}}$	44.47 ± 0.03	4.56 ± 0.31 ms^{-1}	< 1
< Rot. >	**43.87 ± 0.80**		

The mean value is the weighted mean of all the individual measurements. The error of the mean is the standard deviation of the individual measurements divided by the square root of the number of measurements.

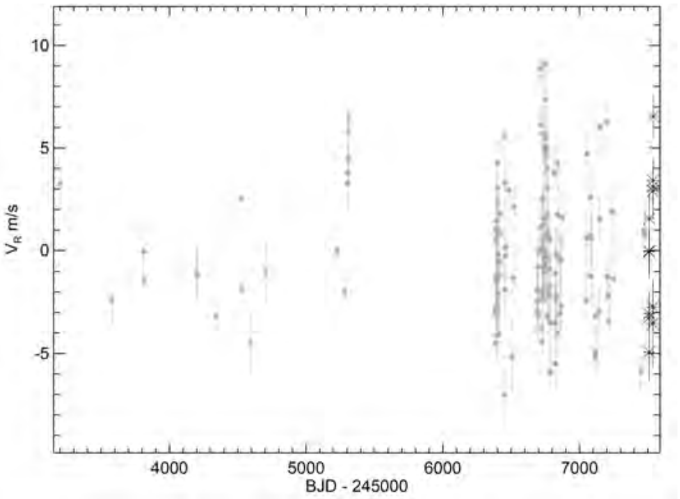

Fig. 8: Radial-velocity time series. Grey dots show HARPS-S data, black asterisks show HARPS-N data.

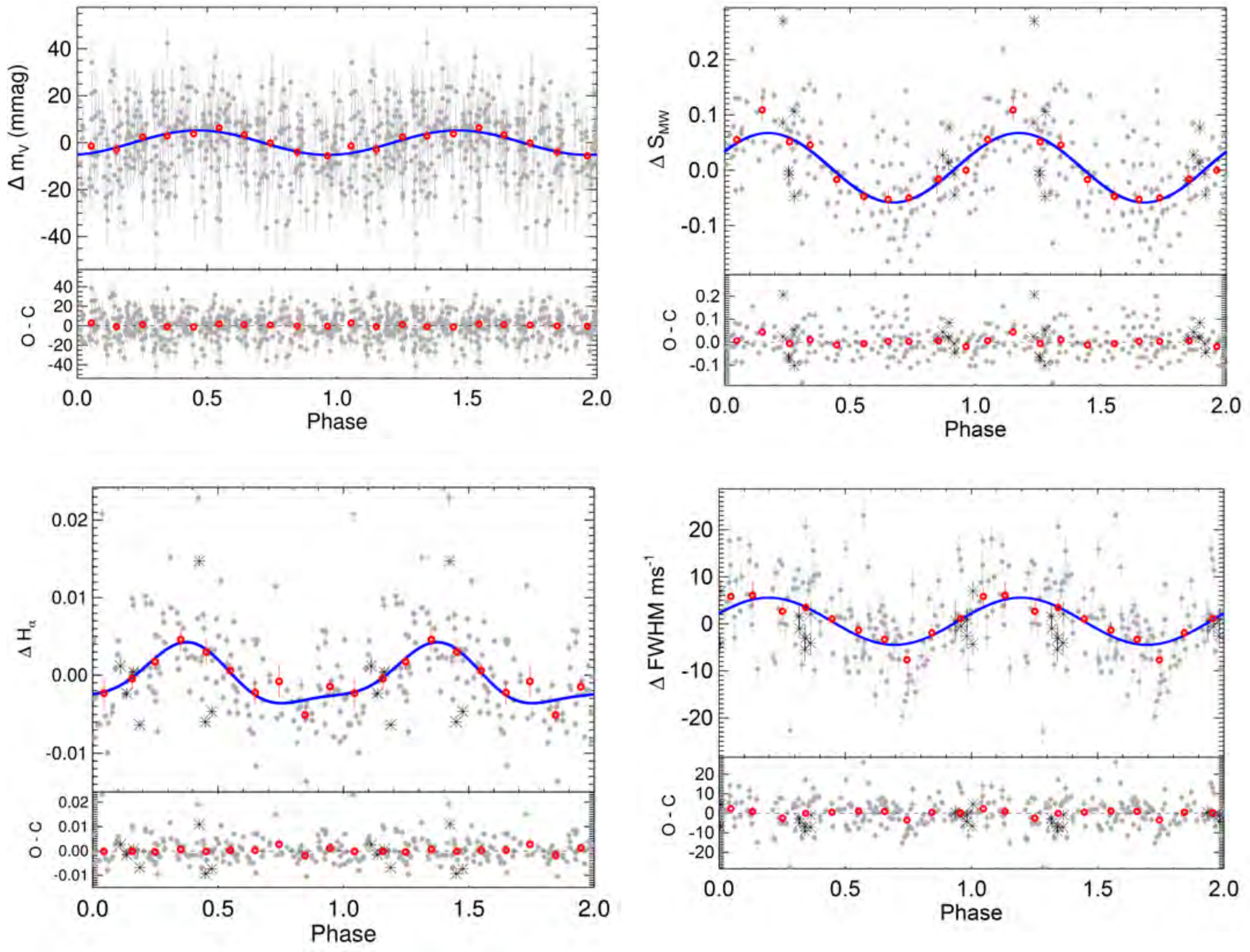

Fig. 7: Phase folded curve using the rotational modulation for the ASAS light curve (upper left), S_{MW} index (upper right), H_α index using a double-harmonic sine curve (lower left) and FWHM (lower right). Grey dots are the raw measurements after subtracting the mean value. Red dots are the same points binned in phase with a bin size of 0.1. The error bar of a given bin is estimated using the weighted standard deviation of binned measurements divided by the square root of the number of measurements included in this bin. This estimation of the bin error bars assumes white noise, which is justified by the binning in phase, which regroups points that are uncorrelated in time.

in the time series and remove them, until there are no more significant signals.

Following this procedure we identify one signal with a false alarm probability much better than the 0.1%, both using the bootstrap and the Cumming (2004) estimates, corresponding to a period of 8.7 d with a semi-amplitude of 2.47 ms^{-1} consistent with circular (Fig. 9 shows the periodogram). Removing this signal leaves a 43.9 d signal with a semi amplitude of 2.86 ms^{-1} and an eccentricity of 0.57, with a false alarm probability better than the 0.1%. No more significant signals are found after removing this two (Fig. 9). Fig. 10 shows the phase folded fits of both the 8.7 d and the 43.9 d signals.

We tested the available dataset for the three ways of calculating the radial velocity, obtaining virtually the same results in every case. Results are shown for the Gaussian + polynomial fit of the cross correlation function.

4.1. Origin of the periodic radial-velocity signals

Stellar activity can induce radial-velocity signals similar to those of Keplerian origin. The inhomogeneities in the surface of the star cause radial-velocity shifts due to the distortion of the spectral line shapes which can, in some cases, create a radial-velocity signal with a periodicity close to the stellar rotation and its first harmonic.

For this star we have a rotation period of 45.39 ± 1.33 d, and two radial-velocity signals of 8.7 d and 43.9 d. The second signal matches almost perfectly the rotation period of the star. On the other hand we do not see in the time series of activity indicators any signal close to the 8.7 d. This is the first evidence of the stellar origin of the 43.9 d signal, and the planetary origin of the 8.7 d signal.

As a second test we measured the Spearman correlation coefficient between the S_{MW}, the H_α index, the FWHM and the radial velocities. We find a significant correlation between all the indexes and the raw radial velocity, which almost disappears

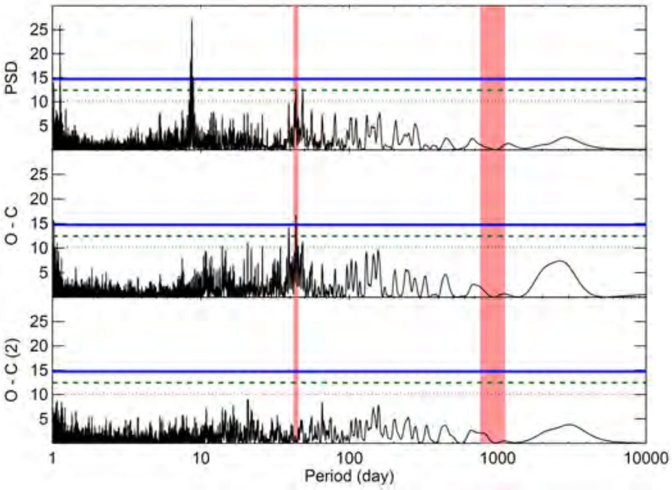

Fig. 9: Periodograms of the radial velocity. Upper panel shows the raw periodogram, middle panel the periodogram of the residuals after subtracting the 8.7 d signal and the lower panel the periodogram of the residuals after subtracting the 43 d signal present in the middle one. Red regions show the periods of the measured rotation and magnetic cycle. Red dotted line for the 10% of false alarm probability, greed dashed line for the 1% and blue thick line for the 0.1%.

when we isolate the 8.7 d signal, and get slightly increased when isolating the 43.9 d signal (see Table. 3). This constitutes a second evidence of the stellar origin of the 43.9 d signal, and of the planetary origin of the 8.7 d one. Following this idea we subtract the linear correlation between the radial velocity and every of the three activity diagnostic indexes. When doing this we see that the strength of the 8.7 d signal remains constant, or even gets increased, while the significance of the 43.9 d gets reduced in all cases (see Fig. 11), even getting buried in the noise after correcting for the correlation with the H_α index.

Keplerian signals are deterministic and consistent in time. When measuring one signal, it is expected to find the significance of the detection increasing steadily with the number of observations, as well as the measured period being stable over time. However, in the case of activity related signal this is not necessarily the case. As the stellar surface is not static, and the configuration of active regions may change in time, changes in the phase of the modulation and in the detected period are expected. Even the disappearance of the signal at certain seasons is possible. Fig. 12 shows the evolution of the false alarm probability of the detection of both isolated signals, as well as the measurement of the most prominent period when isolating them. The 8.7 d signal increases steadily with time, and once it becomes the most significant signal it never moves again. On the other hand the behaviour of the 43.9 d is more erratic, loosing significance during the last observations.

Of the two significant radial-velocity signals detected in our data it seems clear that the one at 8.7 d has a planetary origin, while the one at 43.9 has stellar activity origin.

The shape of the activity induced radial-velocity signal present in our data is evidently not sinusoidal. A double harmonic sinusoidal, as in the case of the activity signals, is the best fit model and the only one that does not create ghost signals after subtracting it. The rotation induced signal is not in phase with the rotation signals in the activity indicators. It appears to be ~45° shifted from the signal in the S_{MW} index and FWHM time series as seen in Bonfils et al. (2007) and Santos et al. (2014). The uncertainty in the phase H_α time series makes it difficult to measure a reliable phase difference.

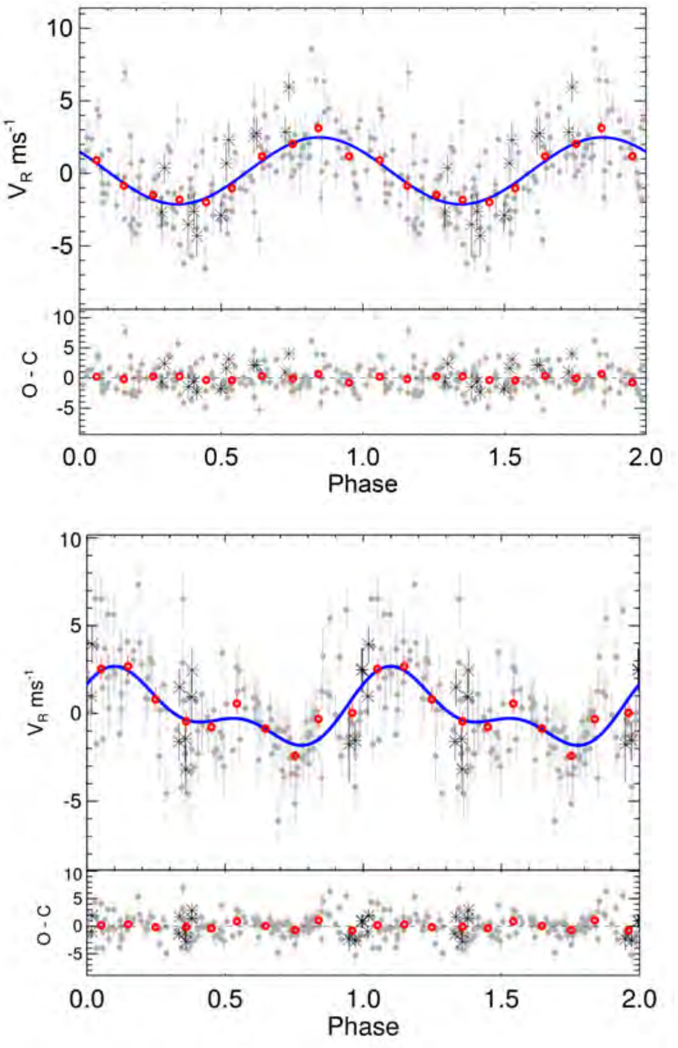

Fig. 10: **Top panel:** Phase folded curve of the radial velocity using the 8.7 d period. Grey dots are the raw radial-velocity measurements after subtracting the mean value and the 43.9 d signal. **Bottom panel:** Phase folded curve of the radial velocity using the 43.9 d period using a double-harmonic sine curve. Grey dots and black asterisks are the raw radial-velocity measurements after subtracting the mean value and the 8.7 d signal. Red dots are the same points binned in phase with a bin size of 0.1. The error bar of a given bin is estimated using the weighted standard deviation of binned measurements divided by the square root of the number of measurements included in this bin. This estimation of the bin error bars assumes white noise, which is justified by the binning in phase, which regroups points that are uncorrelated in time.

Finally an analysis of the spectral window ruled out that the peaks in the periodogram are artefacts of the time sampling alone. No features appear at 8.7 or 43.9 days even after masking the oversaturated regions of the power spectrum. Following Rajpaul et al. (2016) we tried to re-create the 8.7 days signal by injecting the P_{Rot} signal along with a second signal at $P_{Rot}/2$ at 1000 randomized phase shifts with a white noise model. We were never able to generate a signal at 8.7 days, or any signif-

Table 3: Activity - Radial-velocity correlations

Parameter	Raw data	8.7 d signal	43.9 d signal
S_{MW} vs V_R	0.292 ($> 3\sigma$)	0.069 ($<1\sigma$)	0.345 ($> 3\sigma$)
H_α vs V_R	0.338 ($>3\sigma$)	0.113 (1σ)	0.321 ($>3\sigma$)
FWHM vs V_R	0.356 ($> 3\sigma$)	0.164 (1σ)	0.340 ($> 3\sigma$)

Long term variations of activity indicators have been subtracted. The parenthesis value indicates the significance of the correlation given by the bootstrapping process.

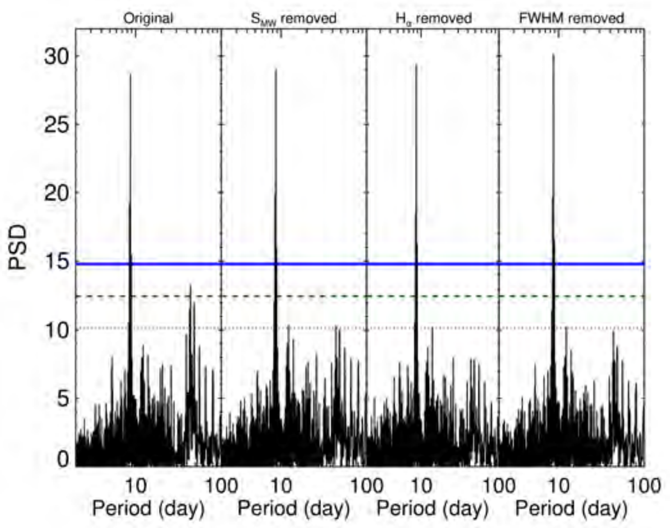

Fig. 11: Periodograms for the radial velocity after removing the correlation with the different activity diagnostic tools. From left to right there is the periodogram for the original data, the periodogram after detrending against the S_{MW} index, against the H_α index, and against the FWHM.

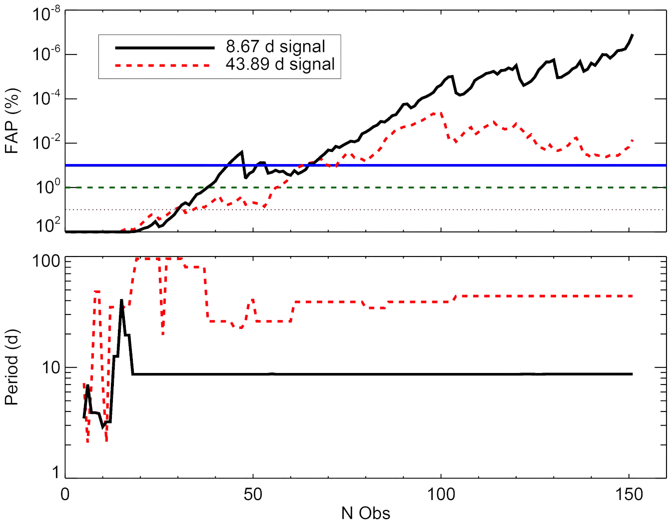

Fig. 12: Evolution of the false alarm probability of the detections (upper panel) for the isolated signals, and stability of the detections (lower panel). Blue thick line shows the behaviour for the 8.7 d signals and red dashed line for the 43.9 d signal.

icant signal at periods close to 8.7 days. It seems very unlikely that any of the signals are artefacts of the sampling.

4.2. GJ 536 b

The analysis of the radial-velocity time series and of the activity indicators leads us to conclude that the best explanation of the observed data is the existence of a planet orbiting the star GJ 536 at the period of 8.7 d, with a semi-amplitude of ~ 2.5 ms^{-1}. The best solution comes from a super-Earth with a minimum mass of 5.3 $M_\oplus$ orbiting at 0.067 AU of its star.

MCMC analysis of the radial-velocity time series

In order to quantify the uncertainties of the orbital parameters of the planet, we perform a bayesian analysis using the code ExoFit (Balan & Lahav 2009). This code follows the Bayesian method described in Gregory (2005); Ford (2005); Ford & Gregory (2007). A single planet can be modelled using the following formula:

$$v_i = \gamma - K[\sin(\theta(t_i + \chi P) + \omega) + e \sin \omega] \quad (3)$$

where γ is system radial velocity; K is the velocity semi-amplitude equal to $2\pi P^{-1}(1 - e^2)^{-1/2} a \sin i$; P is the orbital period; a is the semimajor axis of the orbit; e is the orbital eccentricity; i is the inclination of the orbit; ω is the longitude of periastron; χ is the fraction of an orbit, prior to the start of data taking, at which periastron occurs (thus, χP equals the number of days prior to $t_i = 0$ that the star was at periastron, for an orbital period of P days); and $\theta(t_i + \chi P)$ is the angle of the star in its orbit relative to periastron at time t_i, also called the true anomaly.

To fit the previous equation to the data we need to specify the six model parameters, P, K, γ, e, ω and χ. Observed radial-velocity data, d_i, can be modelled by the equation: $d_i = v_i + \epsilon_i + \delta$ (Gregory 2005), where v_i is the modeled radial velocity of the star and ϵ_i is the uncertainty component arising from accountable but unequal measurement error which are assumed to be normally distributed. The term δ explains any unknown measurement error. Any noise component that cannot be modelled is described by the term δ. The probability distribution of δ is chosen to be a Gaussian distribution with finite variance s^2. Therefore, the combination of uncertainties $\epsilon_i + \delta$ has a Gaussian distribution with a variance equal to $\sigma_i^2 + s^2$ (see Balan & Lahav 2009, for more details).

The parameter estimation in the Bayesian analysis needs a choice of priors. We choose the priors following the studies by Ford & Gregory (2007); Balan & Lahav (2009).The mathematical form of the prior is given in Table 1 and/or 4 of Balan & Lahav (2009). In Table 4, we provide the parameter boundaries explored in the MCMC Bayesian analysis. ExoFit performes 100 chains of 10000 iterations each resulting in a final chain of 19600 sets of global-fit parameters.

We want to simultaneously model the stellar rotation and planetary signals. For that we use the ExoFit to model two RV signals and for the rotation signal we also leave the eccentricity as a free parameter. The posterior distribution of the eccentricity parameter for the rotation signal (not shown in Fig. 13) gives a value of 0.47 ± 0.26. In Fig. 13 we depict the posterior distribution of model parameters, the six fitted parameter, the semi-amplitude velocity, $K_{\rm rot}$ and the period, $P_{\rm rot}$, of the rotation signal, the derived mass of the planet, $m_p \sin i$, and the RV noise given by the s parameter. Most of the parameters show symmetric density profiles except for the eccentricity, e, the longitude of periastron, ω, the fraction χ of the orbit at which the periastron occurs. We note that the density profile of the rotation period displays a tail towards slightly lower values although the rotation period is well defined.

In Table 4 we show the final parameters and uncertainties obtained with the MCMC bayesian analysis with the code ExoFit.

5. Discussion

We detect the presence of a planet with a semi-amplitude of 2.60 m s^{-1} that, given the stellar mass of 0.52 $M_\odot$, converts to m sin *i* of 5.36 $M_\oplus$, orbiting with a period of 8.7 d around GJ 536, an M-type star of 0.52 $M_\odot$ with a rotation period of 43.9 d that shows an additional activity signal compatible with an activity cycle shorter than 3 yr.

The planet is a small super-Earth with an equilibrium temperature 344 K for a Bond albedo A = 0.75 and 487 K for A=0. Following Kasting et al. (1993) and Selsis et al. (2007) we perform a simple estimation of the habitable zone (HZ) of this star. The HZ would go from 0.2048 to 0.3975 AU in the narrowest case (cloud free model) and 0.1044 to 0.5470 AU in the broader one (fully clouded model). This corresponds to orbital periods from 46 to 126 days in the narrower case, and 17 to 204 days in the broader one.

GJ 536 b is in the lower part of the Mass vs Period diagram of known planets around M-dwarf stars (Fig. 14). The planet is too close to the star to be considered habitable. For this star the habitable zone would be from ~20 days to ~ 40 days.

GJ 536 is a quiet early M-dwarf, with a rotation period on the upper end of the stars of its kind (Newton et al. 2016; Suárez Mascareño et al. 2016). Its rotation induced radial-velocity signal has a semi-amplitude of 2.26 ms^{-1} and seems to be stable enough to allow for a clean enough periodogram and to be correctly characterized. The phase of the rotation induced signal seems to be advanced ~45° with respect to the signals in S_{MW} index and FWHM time series. There is a hint for a short activity cycle shorter than 3 yr, which would put it in the lower end of the stars of its kind (Suárez Mascareño et al. 2016), and whose amplitude is so small that would need further follow-up to be properly characterized. The radial-velocity signal induced by this cycle is at this point beyond our detection capabilities.

Given the rms of the residuals there is still room for the detection of more planets in this system, especially at orbital periods longer than the rotation period. Fig. 14 shows the upper limits to the mass of those hypothetical companions. The stability of its rotation signals and the low amplitude of the radial-velocity signals with a magnetic origin makes this star a good candidate to search for longer period planets of moderate mass. A rough estimate of the detection limits tells us there is still room for Earth-like planets (~ 1 $M_\oplus$) at orbits smaller than 10, super-Earths (< 10 $M_\oplus$) at orbits going from 10 to 400 days, and even for a Neptune mass planet (< 20 $M_\oplus$) at periods longer than ~3 yr. Giant planets on the other hand are discarded except for extremely long orbital periods. The time-span of the observations and the RMS of the residuals completely discards the presence of any planet bigger than twice the mass of Neptune with an orbital period shorter than ~ 20 years.

6. Conclusions

We have analysed 152 high resolution spectra and 359 photometric observations to study the presence of planetary companions around the M-dwarf star GJ 536 and its stellar activity. We detected two significant radial-velocity signals, at periods of 8.7 and 43.8 days, respectively.

From the available photometric and spectroscopic information we conclude that the 8.7 d signal is caused by a 5.3 $M_\oplus$ planet with semi major axis of 0.067 AU and equilibrium temperature lower than 500K. The short period of the planet makes it a potential transiting candidate. Detecting the transits would give a new constraining point to the mass-radius diagram.

The second radial-velocity signal of period 43.8 d and semi amplitude of 1.6 ms^{-1} is a magnetic activity induced signal related to the rotation of the star. We also found a magnetic cycle shorter than 3 yr which would place this star among those with the shortest reported magnetic cycles.

We have studied and set limits to the presence of other planetary companions taking into account the rms of the residuals after fitting both the planet and the rotation induced signal. The system still has room for other low mass companions, but planets more massive than Neptune are discarded except at extremely long orbital periods, beyond the habitable zone of the star.

Acknowledgements

This work has been financed by the Spanish Ministry project MINECO AYA2014-56359-P . J.I.G.H. acknowledges financial support from the Spanish MINECO under the 2013 Ramón y Cajal program MINECO RYC-2013-14875. X.B., X.D., T.F. and F.M. acknowledge the support of the French Agence Nationale de la Recherche (ANR), under the program ANR-12-BS05- 0012 Exo-atmos. X.B. and A.W. acknowledge funding from the European Research Council under the ERC Grant Agreement No. 337591-ExTrA. This work was supported by Fundação para a Ciência e a Tecnologia (FCT) within projects reference PTDC/FIS-AST/1526/2014 (POCI-01-0145-FEDER-016886) and UID/FIS/04434/2013 (POCI-01-0145-FEDER-007672). NCS acknowledge support by through Investigador FCT contract of reference IF/00169/2012, and POPH/FSE (EC) by FEDER funding through the program "Programa Operacional de Factores de Competitividade - COMPETE". This work is based on data obtained HARPS public database at the European Southern Observatory (ESO). This research has made extensive use of the SIMBAD database, operated at CDS, Strasbourg, France and NASA's Astrophysics Data System. We are grateful to all the observers of the following ESO projects, whose data we are using: 072.C-0488, 085.C-0019, 183.C-0972 and 191.C-087.

References

Affer, L., Micela, G., Damasso, M., et al. 2016, A&A, 593, A117
Astudillo-Defru, N., Bonfils, X., Delfosse, X., et al. 2015, A&A, 575, A119
Balan, S. T. & Lahav, O. 2009, MNRAS, 394, 1936
Baliunas, S. L., Donahue, R. A., Soon, W. H., et al. 1995, ApJ, 438, 269
Baranne, A., Queloz, D., Mayor, M., et al. 1996, A&AS, 119, 373
Berdyugina, S. V. & Järvinen, S. P. 2005, Astronomische Nachrichten, 326, 283
Berta-Thompson, Z. K., Irwin, J., Charbonneau, D., et al. 2015a, Nature, 527, 204
Berta-Thompson, Z. K., Irwin, J., Charbonneau, D., et al. 2015b, NAT, 527, 204
Bonfils, X., Delfosse, X., Udry, S., et al. 2013, A&A, 549, A109
Bonfils, X., Mayor, M., Delfosse, X., et al. 2007, A&A, 474, 293
Cosentino, R., Lovis, C., Pepe, F., et al. 2012, in SPIE, Vol. 8446, Ground-based and Airborne Instrumentation for Astronomy IV, 84461V
Cumming, A. 2004, MNRAS, 354, 1165
Delfosse, X., Bonfils, X., Forveille, T., et al. 2013, A&A, 553, A8
Delfosse, X., Forveille, T., Perrier, C., & Mayor, M. 1998, A&A, 331, 581
Dressing, C. D. & Charbonneau, D. 2013, ApJ, 767, 95

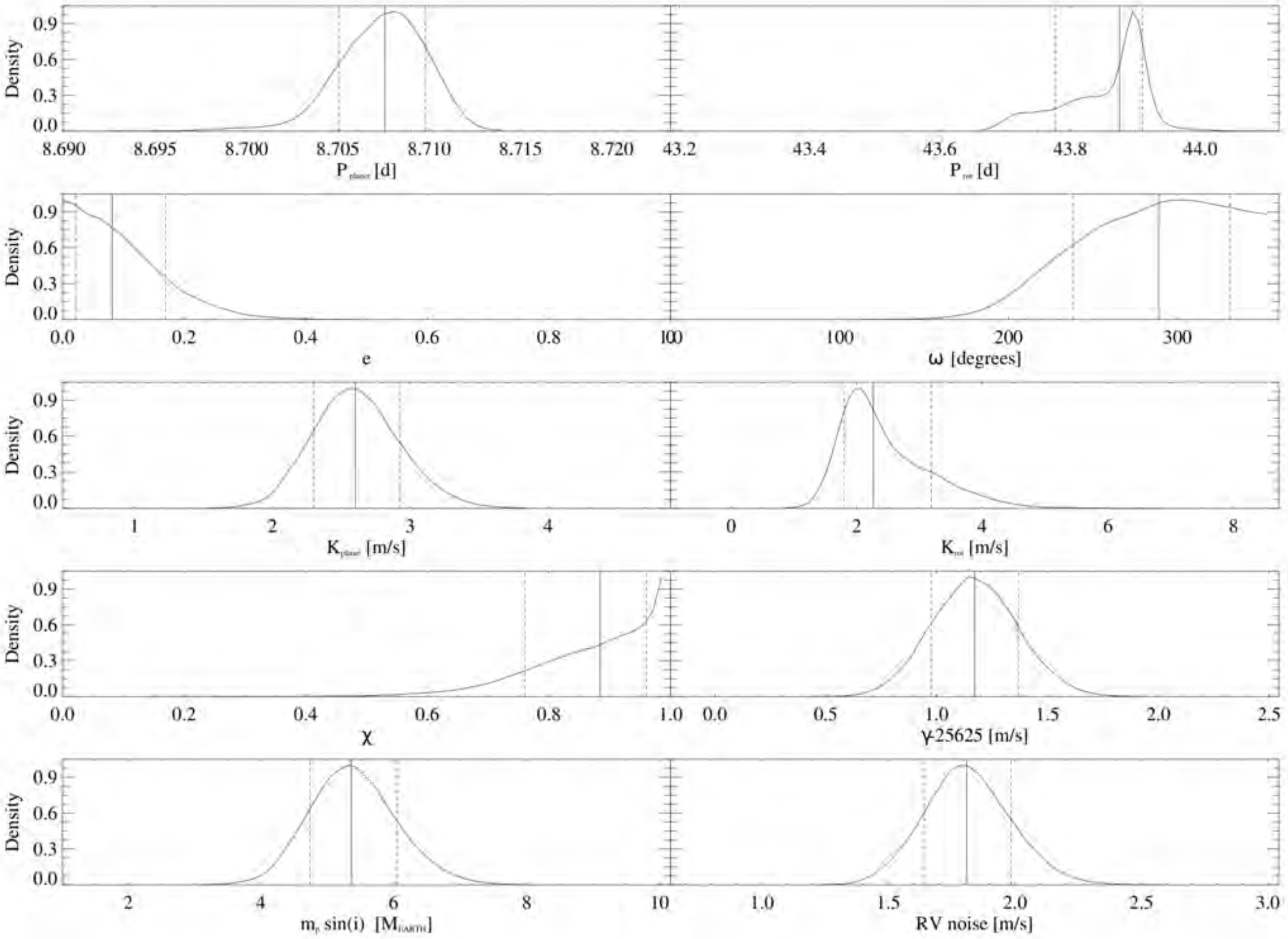

Fig. 13: Posterior distribution of model parameters including the activity signal associated with the rotation period and the orbital parameters of the planet companion of the M dwarf star GJ 536. Vertical dashed line show the median value of the distribution and the dotted lines the 1-σ values.

Table 4: MCMC parameters and uncertainties

Parameter	Value	Upper error	Lower error	Prior
$P_{\rm planet}$ [d]	8.7076	+0.0022	−0.0025	8.3 - 9.0
γ [ms^{-1} – 25625]	1.17	+0.20	−0.20	−5.0 - +5.0
e	0.08	+0.09	−0.06	0.0 - 0.99
ω [deg]	288.7	+42.5	−50.6	0.0 - 360.0
χ	0.88	+0.08	−0.12	0.0 - 0.99
$K_{\rm planet}$ [ms^{-1}]	2.60	+0.33	−0.30	0.0 - 5.0
a [AU]	0.066610	+0.000011	−0.000013	–
$m_p \sin i$ [M$_{\rm Earth}$]	5.36	+0.69	−0.62	–
$P_{\rm rot}$ [d]	43.88	+0.03	−0.10	42.5 - 45.0
$K_{\rm rot}$ [ms^{-1}]	2.26	+0.92	−0.46	0.0 - 7.0
RV noise [ms^{-1}]	1.81	+0.18	−0.17	0.0 - 5.0

Dressing, C. D., Charbonneau, D., & Newton, E. R. 2015, in AAS/Division for Extreme Solar Systems Abstracts, Vol. 3, AAS/Division for Extreme Solar Systems Abstracts, 501.03
Endl, M., Kürster, M., Els, S., Hatzes, A. P., & Cochran, W. D. 2001, A&A, 374, 675
Ford, E. B. 2005, AJ, 129, 1706
Ford, E. B. & Gregory, P. C. 2007, in Astronomical Society of the Pacific Conference Series, Vol. 371, Statistical Challenges in Modern Astronomy IV, ed. G. J. Babu & E. D. Feigelson, 189
Gaidos, E. 2013, ApJ, 770, 90
Gomes da Silva, J., Santos, N. C., Bonfils, X., et al. 2011, A&A, 534, A30
Gregory, P. C. 2005, ApJ, 631, 1198
Horne, J. H. & Baliunas, S. L. 1986, ApJ, 302, 757
Howard, A. W., Johnson, J. A., Marcy, G. W., et al. 2009, ApJ, 696, 75
Howard, A. W., Marcy, G. W., Bryson, S. T., et al. 2012, ApJS, 201, 15
Howard, A. W., Marcy, G. W., Fischer, D. A., et al. 2014, ApJ, 794, 51
Irwin, J., Berta-Thompson, Z. K., Charbonneau, D., Dittmann, J., & Newton, E. R. 2015, in American Astronomical Society Meeting Abstracts, Vol. 225, American Astronomical Society Meeting Abstracts, 258.01

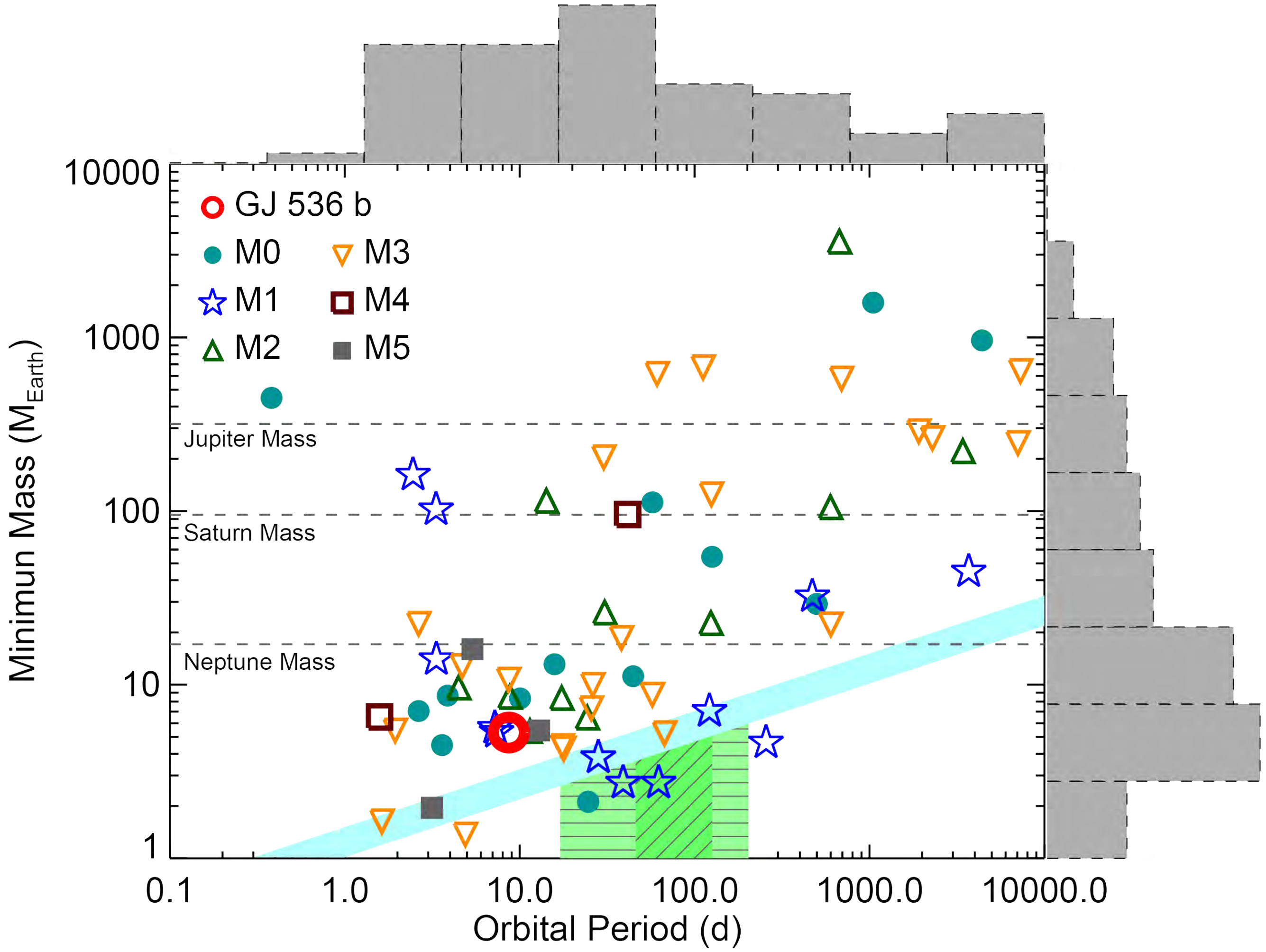

Fig. 14: Minimum mass versus orbital period for the known planets around M-dwarf stars. The red empty dot shows the position of GJ 536 b. Horizontal dashed lines show the mass of the solar system planets for comparison. On the edges of the figure the distribution for each parameter is shown. The cyan shape shows the region where a second planet could exist around GJ 536 (upper limit of the band) and could be detectable given the typical uncertainty of the measurements (lower limit of the band). The green shapes show the habitable region around the star GJ 536. Horizontal lines show the broad scenario while inclined lines show the narrower one.

Kasting, J. F., Whitmire, D. P., & Reynolds, R. T. 1993, ICARUS, 101, 108

Koen, C., Kilkenny, D., van Wyk, F., & Marang, F. 2010, MNRAS, 403, 1949

Kopparapu, R. K. 2013, ApJ, 767, L8

Lovis, C., Dumusque, X., Santos, N. C., et al. 2011, ArXiv e-prints [`arXiv:1107.5325`]

Maldonado, J., Affer, L., Micela, G., et al. 2015, A&A, 577, A132

Marcy, G. W., Butler, R. P., Vogt, S. S., Fischer, D., & Lissauer, J. J. 1998, ApJL, 505, L147

Markwardt, C. B. 2009, in Astronomical Society of the Pacific Conference Series, Vol. 411, Astronomical Data Analysis Software and Systems XVIII, ed. D. A. Bohlender, D. Durand, & P. Dowler, 251

Mayor, M., Bonfils, X., Forveille, T., et al. 2009, A&A, 507, 487

Mayor, M., Marmier, M., Lovis, C., et al. 2011, ArXiv e-prints [`arXiv:1109.2497`]

Mayor, M., Pepe, F., Queloz, D., et al. 2003, The Messenger, 114, 20

Montet, B. T., Crepp, J. R., Johnson, J. A., Howard, A. W., & Marcy, G. W. 2014, ApJ, 781, 28

Newton, E. R., Irwin, J., Charbonneau, D., Berta-Thompson, Z. K., & Dittmann, J. A. 2016, ApJL, 821, L19

Noyes, R. W., Hartmann, L. W., Baliunas, S. L., Duncan, D. K., & Vaughan, A. H. 1984, ApJ, 279, 763

Pepe, F., Mayor, M., Delabre, B., et al. 2000, in SPIE, Vol. 4008, Optical and IR Telescope Instrumentation and Detectors, ed. M. Iye & A. F. Moorwood, 582–592

Pojmanski, G. 1997, ACTAA, 47, 467

Queloz, D., Henry, G. W., Sivan, J. P., et al. 2001, A&A, 379, 279

Rajpaul, V., Aigrain, S., & Roberts, S. 2016, MNRAS, 456, L6

Reiners, A. 2009, A&A, 498, 853

Robertson, P., Endl, M., Henry, G. W., et al. 2015, ArXiv e-prints [`arXiv:1501.02807`]

Robertson, P., Mahadevan, S., Endl, M., & Roy, A. 2014, Science, 345, 440

Saar, S. H. & Donahue, R. A. 1997, ApJ, 485, 319

Santos, N. C., Mortier, A., Faria, J. P., et al. 2014, A&A, 566, A35

Selsis, F., Kasting, J. F., Levrard, B., et al. 2007, A&A, 476, 1373

Suárez Mascareño, A., Rebolo, R., González Hernández, & I., J. 2016, A&A - Submitted

Suárez Mascareño, A., Rebolo, R., González Hernández, J. I., & Esposito, M. 2015, MNRAS, 452, 2745

Udry, S., Bonfils, X., Delfosse, X., et al. 2007, A&A, 469, L43

van Leeuwen, F. 2007, A&A, 474, 653

Waldmeier, M. 1961, The sunspot-activity in the years 1610-1960

Wildi, F., Pepe, F., Chazelas, B., Lo Curto, G., & Lovis, C. 2010, in SPIE, Vol. 7735, Ground-based and Airborne Instrumentation for Astronomy III, 77354X

Wright, D. J., Wittenmyer, R. A., Tinney, C. G., Bentley, J. S., & Zhao, J. 2016, ApJL, 817, L20

Wright, J. & Howard, A. 2012, RVLIN: Fitting Keplerian curves to radial velocity data, Astrophysics Source Code Library

Zechmeister, M. & Kürster, M. 2009, A&A, 496, 577

Zechmeister, M., Kürster, M., & Endl, M. 2009, A&A, 505, 859

Table 5: Full available dataset. Radial velocities are given in the Barycentric Reference Frame after subtracting the secular acceleration. Radial-velocity uncertainties include photon noise, calibration and telescope related uncertainties.

BJD - 2450000 (d)	V_r (ms^{-1})	σ V_r (ms^{-1})	FWHM (Kms^{-1})	BIS Span (ms^{-1})	S_{MW} index	σ S_{MW}	H_α index	σ H_α index	Flag
3202.5590	-25616.5610	1.3488	4444.8091	-5.6623	1.0772	0.0077	0.4960	0.0005	
3579.4972	-25622.4158	1.3573	4448.4550	-5.0540	1.2490	0.0073	0.5058	0.0005	
3811.8370	-25620.2605	1.4564	4438.6871	-9.9863	1.1320	0.0078	0.5043	0.0006	
3813.8047	-25621.7093	1.2228	4433.0342	-8.1469	1.1526	0.0053	0.5047	0.0004	
4196.7394	-25621.5343	1.4416	4443.0970	-6.2410	1.0422	0.0074	0.5001	0.0006	
4202.7156	-25621.6073	1.2951	4425.1466	-6.9079	1.0538	0.0059	0.5039	0.0005	
4340.4836	-25623.6979	1.3024	4429.4257	-7.9120	1.1163	0.0070	0.5076	0.0005	
4525.8756	-25618.1517	1.2817	4433.4956	-11.6982	1.1585	0.0063	0.5069	0.0005	
4528.8393	-25622.4852	1.3126	4433.8369	-5.2346	1.1304	0.0064	0.5044	0.0005	
4591.7914	-25625.2134	1.5565	4442.0880	-7.2876	0.9757	0.0090	0.4940	0.0007	
4703.4993	-25621.8483	1.6802	4433.6780	-10.1303	1.1269	0.0107	0.5032	0.0008	
5226.8854	-25621.1796	1.4632	4446.4284	-10.0405	1.2068	0.0081	0.4996	0.0006	
5281.7491	-25623.1861	1.3854	4428.1838	-8.6441	1.0451	0.0068	0.4889	0.0006	
5305.7265	-25617.9212	1.3201	4427.4995	-9.9302	1.0898	0.0084	0.5030	0.0005	
5306.7140	-25617.4308	1.3665	4430.6156	-8.9673	1.1605	0.0092	0.5063	0.0006	
5307.7196	-25616.7602	1.2588	4436.3939	-10.4465	1.2272	0.0087	0.5109	0.0004	
5308.7013	-25614.7745	1.3191	4446.0321	-8.0523	1.1629	0.0088	0.5039	0.0005	
5309.6925	-25615.3506	1.3031	4442.9390	-8.8002	1.2196	0.0092	0.5080	0.0005	
6385.6469	-25626.3858	1.3821	4428.1616	-3.0622	0.8991	0.0101	0.4978	0.0007	
6386.7448	-25624.9118	1.2594	4425.8662	-9.9115	0.8084	0.0078	0.4935	0.0007	
6387.7815	-25624.7334	1.1527	4424.2671	-8.2783	0.8489	0.0073	0.4952	0.0006	
6388.7254	-25623.3896	1.3647	4416.3803	-7.3567	0.8284	0.0087	0.4964	0.0007	
6389.7264	-25621.3622	1.3006	4421.5546	-11.3118	0.8655	0.0085	0.5048	0.0007	
6390.7371	-25620.4734	1.6898	4419.3411	-9.8647	0.8066	0.0105	0.4943	0.0008	
6391.7497	-25620.8694	1.3286	4424.2490	-11.7541	0.9001	0.0085	0.5003	0.0007	
6393.7913	-25623.1815	1.2910	4415.1907	-7.5922	0.8531	0.0089	0.4978	0.0007	
6394.7750	-25624.4828	1.2851	4429.5659	-9.1806	0.8915	0.0088	0.4949	0.0007	
6395.7000	-25626.0196	1.2787	4417.1293	-9.7255	0.9155	0.0089	0.4957	0.0007	
6396.7103	-25623.1147	1.4092	4424.7395	-12.7127	0.9218	0.0094	0.4968	0.0008	
6397.6863	-25621.0933	1.3000	4423.8606	-9.5686	0.9836	0.0095	0.5064	0.0007	
6398.6799	-25618.8329	1.4313	4426.1457	-7.6371	0.9339	0.0099	0.4992	0.0008	
6399.6958	-25619.5072	1.3309	4440.7943	-9.3043	1.0242	0.0097	0.5024	0.0008	
6400.6899	-25617.6148	1.3276	4426.9125	-10.7879	0.9848	0.0094	0.5022	0.0008	
6401.6532	-25624.7094	1.2229	4430.4209	-8.8857	1.0296	0.0087	0.5028	0.0007	
6402.6436	-25623.9620	1.5248	4430.2528	-9.1200	1.0116	0.0108	0.5027	0.0008	
6403.6245	-25622.1027	1.3310	4443.0225	-9.7811	1.0437	0.0098	0.5032	0.0007	
6404.6425	-25623.0456	1.4532	4434.0050	-10.1067	1.0945	0.0109	0.5106	0.0008	
6410.6262	-25626.0065	1.5706	4448.4592	-8.4057	0.9966	0.0115	0.5039	0.0008	
6414.6393	-25623.0607	1.4853	4439.0697	-6.4884	1.0073	0.0104	0.5072	0.0008	
6415.5922	-25622.4846	2.8093	4434.8839	-17.9962	0.8264	0.0184	0.5053	0.0014	
6415.7332	-25621.0645	1.6543	4445.0213	-9.2692	1.0473	0.0124	0.5114	0.0009	
6416.6954	-25620.1184	1.2661	4431.5240	-4.3249	0.9507	0.0089	0.5034	0.0007	
6451.5800	-25616.3891	1.3405	4433.3694	-16.8458	1.0419	0.0096	0.5063	0.0007	
6452.5545	-25618.6586	1.3803	4434.6138	-8.7892	1.0683	0.0081	0.5099	0.0007	
6454.5556	-25623.8325	1.3937	4431.7379	-9.5482	1.0701	0.0103	0.5075	0.0008	
6455.5374	-25628.9792	1.4965	4422.2962	-7.9232	0.9761	0.0106	0.5020	0.0008	
6458.5877	-25622.2235	1.2855	4423.7546	-11.6472	1.0516	0.0093	0.5101	0.0007	
6460.5668	-25621.7813	1.6473	4431.8028	-10.6556	0.9902	0.0115	0.5048	0.0008	
6481.4839	-25619.0212	1.3733	4419.7151	-8.8134	0.9295	0.0089	0.5034	0.0007	
6508.4718	-25627.1324	1.8094	4441.7103	-10.4168	0.8926	0.0119	0.5119	0.0010	
6514.4694	-25623.2844	1.3027	4424.7201	-6.1677	0.8424	0.0087	0.5033	0.0007	
6521.4589	-25619.8433	1.2696	4431.0487	-10.7298	0.8505	0.0081	0.5007	0.0007	
6690.8780	-25624.1045	1.1926	4422.6617	-9.2806	0.9930	0.0082	0.5063	0.0006	
6691.8339	-25624.6074	1.3498	4426.5396	-8.4985	1.1321	0.0107	0.5168	0.0007	
6692.8139	-25625.0787	1.2900	4431.9081	-10.8969	1.0794	0.0099	0.5048	0.0006	

Table 5: Continued

BJD - 2450000 (d)	V_r (ms^{-1})	σ V_r (ms^{-1})	FWHM (Kms^{-1})	BIS Span (ms^{-1})	S_{MW} index	σ S_{MW}	H_α index	σ H_α index	Flag
6694.8640	-25624.0179	1.1386	4433.0913	-9.0442	1.0415	0.0081	0.5084	0.0006	
6695.8790	-25622.2008	1.1906	4429.7997	-8.1605	1.0384	0.0085	0.5108	0.0006	
6696.8539	-25622.8668	1.3253	4428.3856	-10.0882	1.2174	0.0107	0.5241	0.0007	
6697.7981	-25625.2516	1.3466	4425.1099	-6.5195	1.0566	0.0105	0.5067	0.0007	
6712.8127	-25613.5661	1.3395	4437.9343	-10.5794	1.5124	0.0112	0.5544	0.0008	Rejected
6713.8033	-25613.2583	1.3276	4450.3946	-9.6570	1.2983	0.0109	0.5214	0.0007	
6715.7953	-25620.9555	1.3577	4436.1206	-6.6456	1.2225	0.0106	0.5213	0.0007	
6720.8502	-25616.0066	1.2598	4432.3554	-9.5264	1.1898	0.0094	0.5123	0.0006	
6723.8540	-25622.0386	1.2931	4439.7320	-11.2245	1.2372	0.0103	0.5198	0.0007	
6724.7853	-25624.4497	1.2257	4440.9264	-10.5082	1.2255	0.0097	0.5205	0.0006	
6725.7743	-25624.1936	1.2975	4439.1990	-10.9028	1.1683	0.0103	0.5152	0.0007	
6725.8844	-25626.5410	1.3803	4440.6907	-7.2889	1.1309	0.0105	0.5138	0.0007	
6726.7959	-25625.8960	1.1504	4442.3973	-7.2719	1.0898	0.0084	0.5101	0.0006	
6727.8296	-25620.9225	1.1367	4430.0904	-10.2483	1.0773	0.0079	0.5083	0.0006	
6728.8039	-25621.7110	1.1250	4434.7157	-8.6990	1.0786	0.0080	0.5062	0.0005	
6729.7718	-25616.4237	1.4276	4437.5013	-12.1011	1.0759	0.0085	0.5096	0.0006	
6730.8216	-25619.5981	1.3086	4433.6524	-10.6152	1.0424	0.0095	0.5111	0.0007	
6732.7980	-25622.9502	1.4351	4421.7672	-4.3220	1.0392	0.0101	0.5106	0.0008	
6737.8572	-25620.5708	1.3554	4428.3888	-5.4130	1.0060	0.0093	0.5102	0.0007	
6738.8726	-25622.5574	1.2338	4431.8640	-7.8770	0.9898	0.0086	0.5047	0.0007	
6739.8058	-25622.1678	1.1512	4425.2586	-9.5216	1.0135	0.0078	0.5075	0.0006	
6740.8311	-25624.4843	1.0987	4428.1852	-6.4714	0.9862	0.0073	0.5061	0.0005	
6741.7462	-25623.9200	1.1678	4429.0187	-9.0739	1.0092	0.0081	0.5038	0.0006	
6742.8207	-25623.1636	1.1028	4426.1406	-9.8389	1.0343	0.0076	0.5094	0.0005	
6743.7632	-25622.7840	1.2011	4432.8256	-6.7370	1.0186	0.0084	0.5069	0.0006	
6745.7321	-25617.2597	1.1588	4423.0781	-11.4489	1.0638	0.0081	0.5124	0.0007	
6746.8203	-25613.0541	1.2944	4428.6487	-8.3582	1.0296	0.0090	0.5158	0.0007	
6752.8315	-25621.4802	1.3848	4432.6911	-7.1023	1.0633	0.0106	0.5210	0.0008	
6754.8603	-25617.1072	2.0773	4434.8424	-14.7497	1.1186	0.0161	0.5213	0.0011	
6755.8430	-25617.0817	2.0606	4444.2810	-9.2983	1.0480	0.0157	0.5182	0.0011	
6755.8530	-25614.7730	1.9338	4449.5330	-8.2994	1.1561	0.0154	0.5220	0.0010	
6756.8521	-25616.6832	1.0939	4440.9586	-9.8160	1.1383	0.0085	0.5169	0.0005	
6757.8085	-25617.4805	1.4014	4441.8165	-9.7412	1.1327	0.0112	0.5181	0.0007	
6758.8266	-25622.4824	2.2098	4438.0807	-15.1975	1.0999	0.0174	0.5266	0.0012	
6759.8277	-25621.4838	1.3814	4438.3218	-7.9763	1.1324	0.0111	0.5192	0.0007	
6760.8142	-25620.2626	1.3119	4448.0559	-8.2829	1.5703	0.0125	0.5642	0.0007	Rejected
6763.7243	-25620.4110	1.0500	4442.6357	-10.9225	1.1538	0.0073	0.5130	0.0005	
6764.7765	-25618.1639	1.2340	4444.4456	-9.9255	1.1184	0.0092	0.5128	0.0006	
6765.7208	-25619.0905	1.3628	4437.2341	-6.5105	1.1466	0.0078	0.5131	0.0006	
6766.7265	-25621.2292	1.0945	4439.1904	-9.8447	1.2270	0.0081	0.5229	0.0005	
6767.6534	-25623.9784	1.5745	4433.4716	-10.2058	1.1048	0.0115	0.5113	0.0008	
6768.6678	-25625.3559	1.2107	4429.1243	-7.0854	1.0659	0.0087	0.5089	0.0006	
6778.6271	-25624.2948	1.3732	4424.6235	-8.2880	0.9981	0.0077	0.5003	0.0005	
6779.7560	-25623.0220	1.5571	4433.6733	-7.6866	0.9779	0.0094	0.5036	0.0007	
6781.6011	-25621.5230	1.5651	4434.4575	-9.5425	0.9537	0.0096	0.5022	0.0007	
6782.6156	-25621.6172	1.3793	4433.3780	-4.7485	1.1337	0.0085	0.5159	0.0005	
6784.6137	-25625.6796	1.2493	4430.6030	-6.3606	0.9865	0.0089	0.5079	0.0006	
6785.5546	-25623.9276	1.5364	4411.9798	-7.3440	0.9995	0.0118	0.5097	0.0008	
6786.6679	-25628.0817	1.1219	4420.8351	-8.7321	0.9403	0.0073	0.5038	0.0005	
6814.7183	-25618.4375	1.3822	4442.1718	-6.9710	1.0105	0.0109	0.5029	0.0007	
6822.5823	-25625.6969	1.6325	4427.8930	-14.3619	1.0863	0.0119	0.5063	0.0009	
6823.5834	-25627.6799	1.3314	4432.6413	-9.5886	1.0479	0.0097	0.5004	0.0007	
6824.5777	-25623.2701	1.4221	4430.6359	-9.1015	1.0257	0.0097	0.4996	0.0007	
6825.6520	-25622.3060	1.3593	4435.5327	-7.2742	1.0811	0.0105	0.5055	0.0007	
6826.5764	-25621.9304	1.2330	4428.6392	-4.9112	1.3187	0.0094	0.5315	0.0007	Rejected
6827.5754	-25624.3321	1.1535	4432.4085	-6.5820	1.0300	0.0082	0.5024	0.0006	
6828.6006	-25624.5384	1.1901	4429.2042	-10.7163	1.1152	0.0086	0.5094	0.0006	
6838.5568	-25626.1804	1.1653	4430.8116	-10.7542	1.0408	0.0083	0.5163	0.0006	
6839.5704	-25622.4896	1.4164	4425.8922	-8.3993	0.9890	0.0105	0.5122	0.0006	
6840.5286	-25620.4583	1.4235	4421.9119	-7.9951	0.9953	0.0097	0.5107	0.0007	

Table 5: Continued

BJD - 2450000 (d)	V_r ($\mathrm{ms^{-1}}$)	σ V_r ($\mathrm{ms^{-1}}$)	FWHM ($\mathrm{Kms^{-1}}$)	BIS Span ($\mathrm{ms^{-1}}$)	S_{MW} index	σ S_{MW}	H_α index	σ H_α index	Flag
6841.6035	-25614.8073	2.5202	4438.8469	-2.9369	1.1631	0.0220	0.5331	0.0013	Rejected
6842.4896	-25617.9822	1.3193	4436.3770	-9.2662	1.0293	0.0094	0.5150	0.0007	
6857.5388	-25625.2710	1.7446	4421.9564	-10.6323	1.0678	0.0125	0.5036	0.0009	
6858.5182	-25622.6933	1.4250	4432.2060	-9.9027	1.0034	0.0099	0.4929	0.0007	
6863.5169	-25622.6876	1.3877	4434.8193	-7.8466	1.0297	0.0103	0.5056	0.0007	
6864.5176	-25624.8996	1.1102	4424.7214	-8.4713	0.9533	0.0077	0.4994	0.0005	
6874.4791	-25620.6138	1.6580	4440.2229	-5.6786	1.0463	0.0121	0.5086	0.0009	
7047.8603	-25624.7545	1.2191	4434.2142	-8.8214	1.0933	0.0090	0.5089	0.0006	
7053.8561	-25621.7439	1.4441	4446.4398	-7.8204	1.0895	0.0103	0.5060	0.0007	
7057.8269	-25622.0109	1.4588	4452.3988	-8.1500	1.5121	0.0123	0.5507	0.0008	Rejected
7058.8515	-25617.6495	1.8982	4442.7452	-17.1716	1.0415	0.0136	0.5044	0.0010	
7079.8236	-25619.7617	1.2772	4436.6205	-11.9584	1.1289	0.0094	0.5148	0.0007	
7080.8500	-25621.6358	1.4059	4427.7199	-5.2545	1.0410	0.0100	0.5063	0.0007	
7082.8651	-25623.5924	1.1403	4434.4908	-7.9841	1.0022	0.0078	0.5025	0.0006	
7085.7333	-25621.7323	1.2833	4430.9624	-8.7143	1.0902	0.0098	0.5114	0.0006	
7114.8209	-25625.5802	1.4614	4410.2902	-14.3900	0.9577	0.0102	0.5028	0.0008	
7115.7150	-25627.5907	1.3311	4428.5220	-8.7149	1.0657	0.0092	0.5075	0.0007	
7116.7852	-25627.3237	1.2820	4424.2680	-7.4215	0.9395	0.0083	0.5014	0.0007	
7142.7719	-25625.3593	1.2290	4428.5104	-8.7045	0.9850	0.0083	0.5065	0.0006	
7147.7808	-25616.3909	1.3538	4441.0481	-9.6390	0.9792	0.0103	0.5038	0.0007	
7148.7468	-25620.8954	1.2741	4429.2924	-10.0502	0.9918	0.0094	0.5001	0.0006	
7202.5939	-25616.1481	1.6565	4441.1922	5.6209	0.9188	0.0097	0.4982	0.0008	
7204.6007	-25623.6987	1.4010	4452.3792	2.2721	0.9045	0.0081	0.4978	0.0006	
7211.5712	-25624.5994	1.3200	4447.6138	2.6096	0.8998	0.0075	0.4998	0.0005	
7212.6084	-25624.9280	5.6243	4437.5059	-12.1776	0.4064	0.0213	0.5013	0.0024	
7214.5883	-25625.9395	2.0090	4454.7852	5.6477	0.8619	0.0135	0.5093	0.0010	
7238.5220	-25620.5551	1.4908	4444.8883	4.9186	0.9594	0.0104	0.5031	0.0006	
7249.4828	-25623.8234	1.8006	4447.2116	4.2354	0.8713	0.0112	0.4972	0.0008	
7448.8620	-25628.4475	1.4117	4457.4186	6.7720	0.9810	0.0103	0.5065	0.0007	
7473.8467	-25621.6222	1.1138	4455.5312	0.5160	0.9392	0.0082	0.5075	0.0005	
7476.8649	-25621.8943	1.1800	4459.2948	3.4832	0.9172	0.0083	0.5028	0.0006	
7508.4799	-25624.9467	1.0813	4467.1596	-5.9534	1.0357	0.0107	0.5091	0.0005	HARPS-N
7508.5698	-25621.9227	1.0769	4464.6067	-7.1361	1.2192	0.0108	0.5287	0.0005	HARPS-N
7509.4759	-25625.1223	1.2681	4460.0000	-9.6134	0.9486	0.0111	0.4974	0.0005	HARPS-N
7509.5684	-25626.8176	1.4120	4462.4128	-8.3783	0.9415	0.0128	0.4969	0.0006	HARPS-N
7510.4709	-25621.9484	1.3119	4461.3527	-5.7705	0.9028	0.0117	0.4927	0.0006	HARPS-N
7510.5488	-25620.3344	1.2794	4467.5365	-5.4813	1.0562	0.0124	0.5053	0.0006	HARPS-N
7535.4250	-25625.4364	2.1712	4464.4853	-2.7902	0.9369	0.0239	0.5095	0.0012	HARPS-N
7536.4320	-25624.6383	1.1442	4463.1872	-8.4287	0.9829	0.0134	0.5065	0.0006	HARPS-N
7537.4339	-25619.0095	1.3012	4461.0889	-10.0375	0.9686	0.0148	0.5083	0.0007	HARPS-N
7537.5223	-25618.7979	1.1950	4464.6137	-6.3194	1.0328	0.0149	0.5105	0.0007	HARPS-N
7538.4145	-25618.5006	1.0871	4459.3290	-6.8755	0.9491	0.0118	0.5029	0.0006	HARPS-N
7538.5184	-25615.3666	1.0356	4470.6070	-7.3075	0.9111	0.0099	0.5017	0.0005	HARPS-N